JOURNAL OF MATERIALS SCIENCE 10 (1975) 113–122

Microfracture beneath point indentations in brittle solids

B. R. LAWN*
Division of Materials Science, School of Applied Sciences, University of Sussex, Falmer, Sussex UK
M. V. SWAIN†
School of Physics, University of New South Wales, Kensington, New South Wales, Australia

The microfracture patterns observed around point indentations in brittle solids are investigated. A description is first given of the stress field in an elastic half-space loaded normally at a point in its surface. This field is then used as a basis for analysing the crack geometry. A localized zone of irreversible deformation forms about the contact point, thereby removing a singularity in the elasticity solutions and providing nucleation centres for the ensuing microcracks. Generally, two main types of 'vent' cracks are observed to propagate from the deformation zone: median vents, formed during indenter loading, spread downward below the point of contact on planes of symmetry, and lateral vents, formed during unloading, spread sideways toward the specimen surface. Of these, the median vent is relatively well-behaved, and is amenable to standard fracture-mechanics analysis. From such an analysis we derive the means for predetermining, in principle, the depth of fracture damage under given point loading conditions. The significance of the results in relation to important practical applications, such as glass cutting and surface fragmentation processes, is discussed.

1. Introduction

Point-indentation techniques, long used as a basis for routine hardness testing (e.g. Vickers pyramid test, Knoop test), are finding increasing application in the study of the mechanical properties of brittle solids. The particular attraction of these techniques lies in their unique simplicity as a nondestructive means for producing regions of high stress intensity in a specimen. Moreover, the indentation stress field is dominated by components of shear and hydrostatic compression, a situation favourable to the operation of such irreversible deformation modes as plastic flow and structural densification; it is, of course, this irreversible deformation which accounts for the residual impression left by the indenter. The same modes may never have an opportunity to manifest themselves in a more conventional mechanical test arrangement, for it is difficult to safeguard against premature brittle failure of the test-piece due to the inevitable presence of substantial tensile stresses, either directly applied or spurious. Indeed, for the most brittle solids the point-indentation test affords the only practical method for characterizing yield, or densification, parameters.

However, while the component of tension in the indentation field itself is relatively small, it is by no means insignificant. Thus, depending on the degree of brittleness of a given material, one might expect to find a certain amount of microcracking around the immediate deformation zone. Observations of indentation-induced microfracture are in fact commonplace in such solids as the diamond-structure crystals, silicates (e.g. quartz, fused silica), ceramics (e.g. sapphire), and intrinsically strong metals and alloys (e.g. tungsten, nitrides). In most applications of indentation testing, the incidence of microcracking is regarded as having little more

---

*On study leave, from School of Physics, University of New South Wales, Kensington, New South Wales, Australia.

†Present address: Martin Marietta Laboratories, Martin Marietta Corporation, South Rolling Road, Baltimore, Maryland, USA.

than nuisance value because of disruptive effects on the overall deformation pattern. But there are some areas of materials research in which these fracture processes have a vital bearing. One such area concerns the use of concentrated loading techniques for introducing well-defined cracks into a solid in a controlled manner; this is of particular relevance to glass-cutting operations, where a sharp scribing tool is used to produce a linear starting crack. Another area relates to the mechanisms of comminution (particle fragmentation) of brittle materials; here, the indentation test may be used as a useful model system for simulating individual damage events in abrasion, grinding and erosion processes.

It is the purpose of this paper to investigate the mechanics of point-indentation microfracture. A complete description would embrace both *initiation* and *propagation* stages of crack growth. The initiation stage is a complex problem in its own right, involving such factors as deformation mode (which may in turn depend on the specimen history and microstructure), indenter geometry, etc.; we shall avoid explicit consideration of this issue, assuming only that suitable initiation centres do exist within the indentation zone. The ensuing propagation stage, on the other hand, is readily amenable to a more or less standard fracture mechanics analysis in terms of a well-defined applied stress field and fracture surface energy parameter; with this approach we can explain the essential features of microcrack patterns observed in indented glass and other brittle materials.

2. Stress field beneath ideal pointed indenter

We consider the stress situation in an elastic half-space subjected to a normal point load P, Fig. 1. This is the so-called Boussinesq problem, the solution of which is summarized in the Appendix. For an isotropic material of Poisson's ratio ν, the stress components in the curvilinear coordinate system of Fig. 1 are seen to assume the simple, general form

$$\sigma_{ij} = (P/\pi R^2)\,[f_{ij}(\phi)]_\nu\,. \qquad (1)$$

Thus, at fixed indenter load, the stress field varies as the inverse square of the radial distance from the contact point, times an independent angular term.

The relevant features of the Boussinesq stress field are illustrated in Figs. 2 to 4, for the case $\nu = 0.25$. In Fig. 2 we plot *trajectories* of the three principal normal stresses, σ_{11}, σ_{22}, σ_{33}; that is, curves whose tangents indicate the *directions* of the principal stresses at each point. The three families of trajectories are labelled such that $\sigma_{11} \geqslant \sigma_{22} \geqslant \sigma_{33}$ nearly everywhere in the field. In Fig. 3 we plot *contours* of these principal stresses; the curves represent polar functions $R_{ii}(\phi)$ obtained from Equation 1 at σ_{ii} = con-

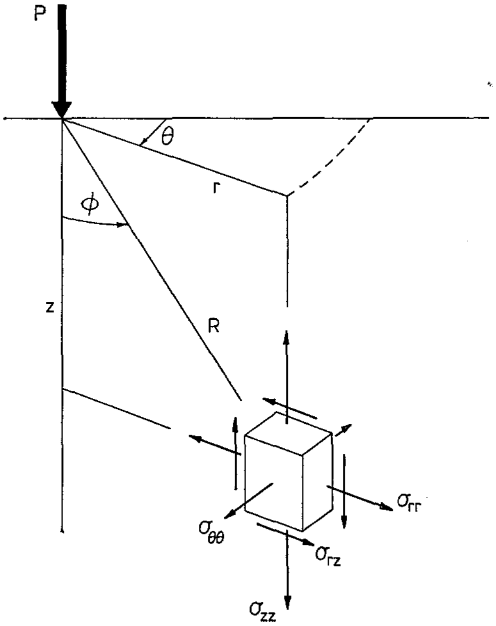

Figure 1 Coordinate system for axially symmetric point loading P. Expressions for the stress components indicated are given in the Appendix.

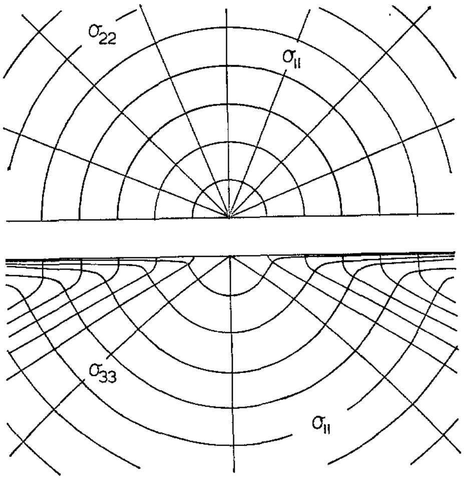

Figure 2 Half-surface view (top) and side view (bottom) of stress trajectories in Boussinesq field. Plotted for $\nu = 0.25$.

stant, and accordingly indicate the *distribution* of the principal stresses. Both σ_{11} and σ_{33} are contained within planes of symmetry through the normal load axis, with σ_{11} everywhere tensile, σ_{33} everywhere compressive. σ_{22} is a 'hoop stress', tensile within a conical region $\phi < 51.8°$ below the indenter and compressive outside this region. The relative *magnitudes* of the three principal normal stresses are shown to better advantage in Fig. 4a, in which just the angular function of Equation 1 are plotted. Similar plots are given for the maximum principal shear stress and hydrostatic compression in Fig. 4b. (It is noted that σ_{33} actually exceeds σ_{22} in a shallow surface region $\phi > 77.2°$, whence σ_{12} replaces σ_{13} as the maximum shear stress.)

It would thus appear that, given favourable initiation conditions, the tensile component of the point-indentation field might well be sufficiently large to sustain a brittle crack. In this context the value of Poisson's ratio becomes an important consideration. Whereas the maximum principal shear and hydrostatic compression are insensitive to variations in this term, the same is not true of the tensile stress; indeed, at $\nu = 0.5$ the tensile component disappears completely. As it turns out, over the range $\nu = 0.2$ to 0.5 materials generally tend to vary from highly brittle to highly ductile [1]; our chosen value of $\nu = 0.25$ above thus lies toward the brittle end of the spectrum, as required.

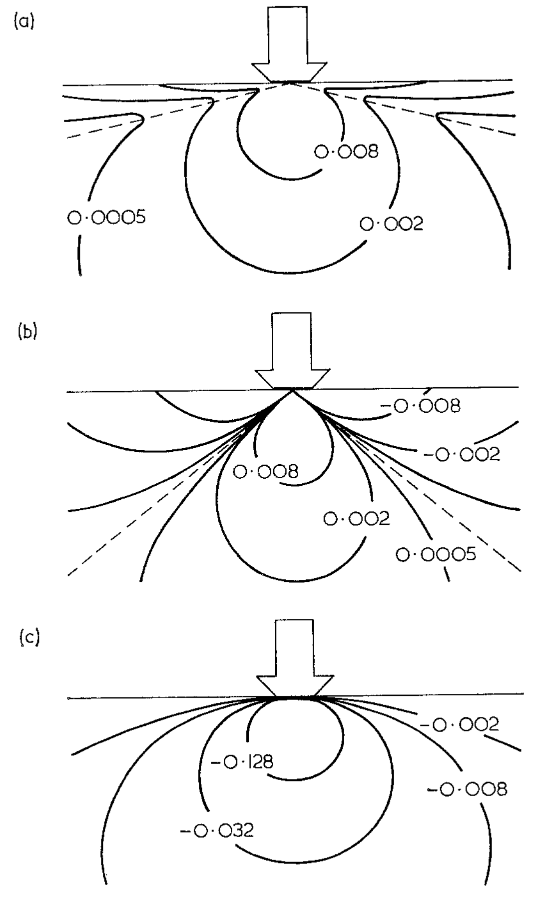

Figure 3 Contours of principal normal stresses (a) σ_{11}; (b) σ_{22}; (c) σ_{33} in Boussinesq field, shown in plane containing contact axis. Plotted for $\nu = 0.25$. Unit of stress is p_0, contact "diameter" (arrowed) is $2a\sqrt{\alpha}$ (see Equations 1 to 3). Note sharp minimum in σ_{11} and zero in σ_{22}, indicated by broken lines in (a) and (b) respectively.

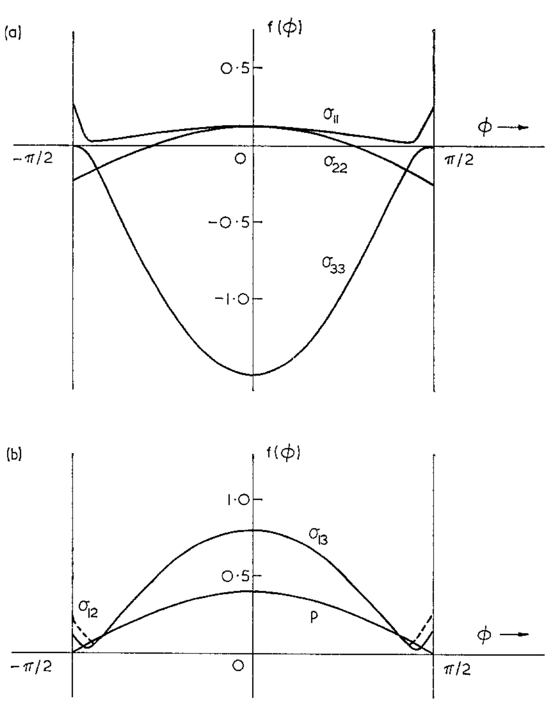

Figure 4 Angular variation of principal stress components in Boussinesq field, plotted in terms of dimensionless function $f(\phi)$ (Equation 1). (a) Principal normal stresses, σ_{11}, σ_{22}, σ_{33}; (b) maximum principal shear stress, σ_{13} or σ_{12} (broken line), and hydrostatic compression, p. Plotted for $\nu = 0.25$.

We should finally note that the stress-field Equation 1 contains a singularity at the contact origin $R = 0$. The idealized picture of an applied load supported by a point contact strictly needs to be replaced by a model which makes provision for indenter support over a non-zero contact area. Physically, one envisages a mechanism of load redistribution in which the intense stresses in the immediate vicinity of a sharp indenter are relieved by the operation of nonlinear, irreversible deformation processes. It becomes convenient to represent the scale of the contact zone by some characteristic dimension a, such that the mean contact pressure may be written

$$p_0 = P/\alpha\pi a^2\,, \qquad (2)$$

where α is a dimensionless constant determined by indenter geometry. Then division of Equation 2 into Equation 1 suitably normalizes the field parameters;

$$\sigma_{ij}/p_0 = \alpha(a/R)^2\,[f_{ij}(\phi)]\nu\,. \qquad (3)$$

(For a pointed indenter which leaves a geometrically similar impression in a homogeneous specimen at all loads, the mean indentation pressure remains invariant and accordingly provides a measure of the *hardness* of the material [2].) Some feeling for the influence of this effective 'indenter-tip blunting' on the field may be gained from Fig. 5, where the elastic stress term $\sigma_{\theta\theta}$ along the contact axis is plotted for both Boussinesq point loading and Hertzian circular contact loading [3]; here we take a to be the contact radius, giving $\alpha = 1$ in the above equations. It is evident that the representations of Figs 2 to 4 retain their validity only at distances far removed from the contact zone, i.e. $R \gg a$ (St. Venant's principle).

3. Microfracture geometry

Observations have been made of indentation-induced microcracking under a wide range of experimental conditions in an attempt to establish a general pattern of behaviour [4]. Materials investigated include silicon, quartz, fused silica, soda-lime glass, and others. The pointed indenters, all diamond, ranged from those used in standard hardness testing, e.g. Vickers pyramid and Knoop, to specially ground cones. Specimens were prepared in slab-like form, with their test surfaces finely polished. Commercial testing machines, viz. Zwick Hardness Testing Machine (0-100N) and Instron Universal Testing Machine (0-1000N), were used to load the indenter onto the specimen. Microscopic examination of the cracking was carried out after *and* (whenever appropriate) during the indentation process. The tests were mainly conducted in ordinary laboratory atmosphere, but a small proportion were conducted in contrived environments.

Although the microfracture geometry observed showed many variants, a general pattern did emerge. We describe the essential features of this pattern with reference to the schematic representation in Fig. 6, delaying discussion of any complications for the present. The sequence depicts one complete loading and unloading cycle:

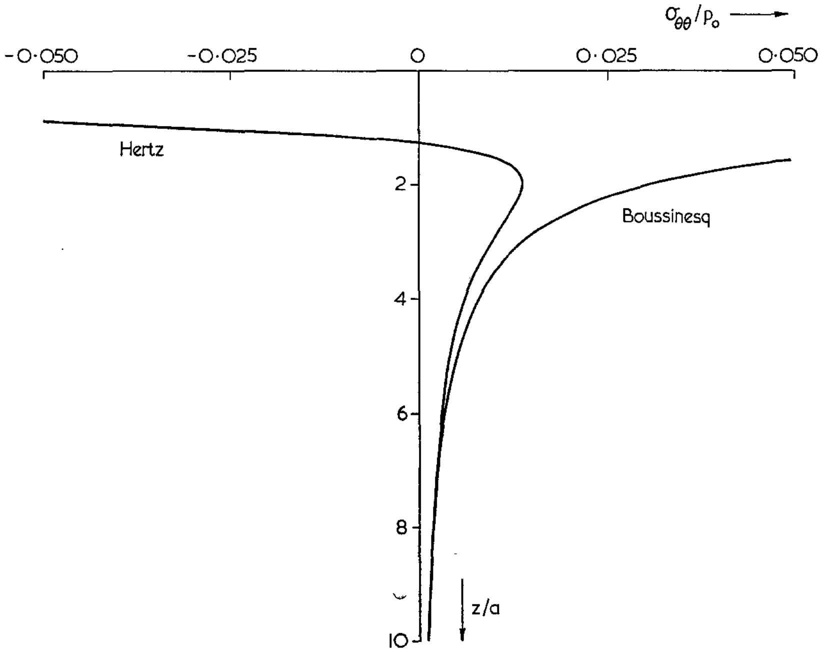

Figure 5 Comparison plot of $\sigma_{\theta\theta}(z)$ stress term for Boussinesq and Hertzian fields. Plotted for $\nu = 0.25$. Note divergence of curves in vicinity of contact zone (at $z \to 0$, $\sigma_{\theta\theta} \to \infty$ in the Boussinesq field, $\sigma_{\theta\theta} \to -1.125\,p_0$ in the Hertzian field).

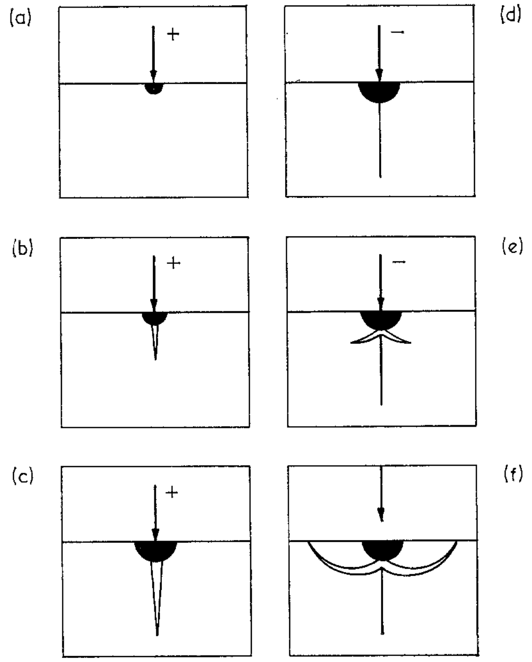

Figure 6 Schematic of vent crack formation under point indentation. Median vent forms during loading (+) half-cycle, lateral vents during unloading (−) half-cycle. Fracture initiates from deformation zone (dark region). See text.

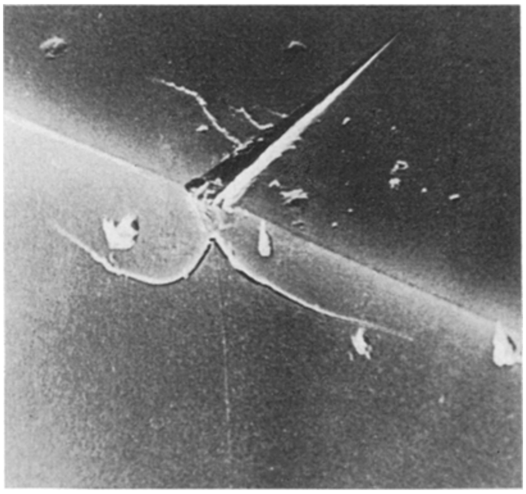

Figure 7 Scanning electron micrograph of Knoop impression in quartz (0001) surface. Section obtained by indenting across a fortuitous hairline crack in the specimen, and subsequently propagating the crack through the material. Note deformation zone immediately below surface impression, and associated vent pattern. Note also that lateral vents show wider residual interface separation than median vent. Indenter load 2 N, width of field 100 μm.

(a) *Initial loading* The sharp indenter induces a zone of irreversible deformation about the contact point. The size of this zone increases with load, according to Equation 2 with p_0 = constant.

(*b*) *Critical zone formation* At some critical indenter load a crack suddenly initiates below the contact point, where the stress concentration is greatest. This crack, commonly termed the *median vent*, lies on a plane of symmetry in the applied field, the specific θ-orientation of which depends on such factors as indenter geometry and crystal anisotropy.

(c) *Stable crack growth* Increasing the load causes further, stable extension of the median vent.

(d) *Initial unloading* The median vent begins to close (but not heal).

(e) *Residual-stress cracking* Relaxation of deformed material within the contact zone just prior to removal of the indenter superimposes intense residual tensile stresses upon the applied field. Sideways-extending cracks, termed *lateral vents*, begin to appear.

(f) *Complete unloading* Lateral vents continue to extend, and may cause chipping.

These general features are clearly evident in the micrographs of Figs. 7 and 8. The effect of reloading the indenter onto the impression is to *close* the lateral vents, and simultaneously to *reopen* the median vents.

It can be readily argued on thermodynamic grounds that the ultimate history of a brittle fracture in an elastically loaded body is predetermined by the tensile stress field before propagation has even begun [5]. This type of argument has a particularly useful application in the general elastic contact problem, as has been demonstrated in detail for the growth of a cone crack in the Hertzian field [6]. Essentially, a crack, once initiated, will at any point tend to propagate along trajectories of lesser principal normal stresses, thereby maintaining near-orthogonality to a major tensile component. It follows that a crack initiated directly below the point of a sharp indenter will tend to grow straight downward along the axial σ_{33} trajectory (Fig. 2), as depicted in Fig. 6b and c, orthogonally to the tensile stress $\sigma_{11} = \sigma_{22} = \sigma_{\theta\theta}$ at $\phi = 0$ (Fig. 4). The same crack will also tend to expand sideways in a plane θ = constant along the σ_{11} trajectory, orthogonally everywhere to the hoop

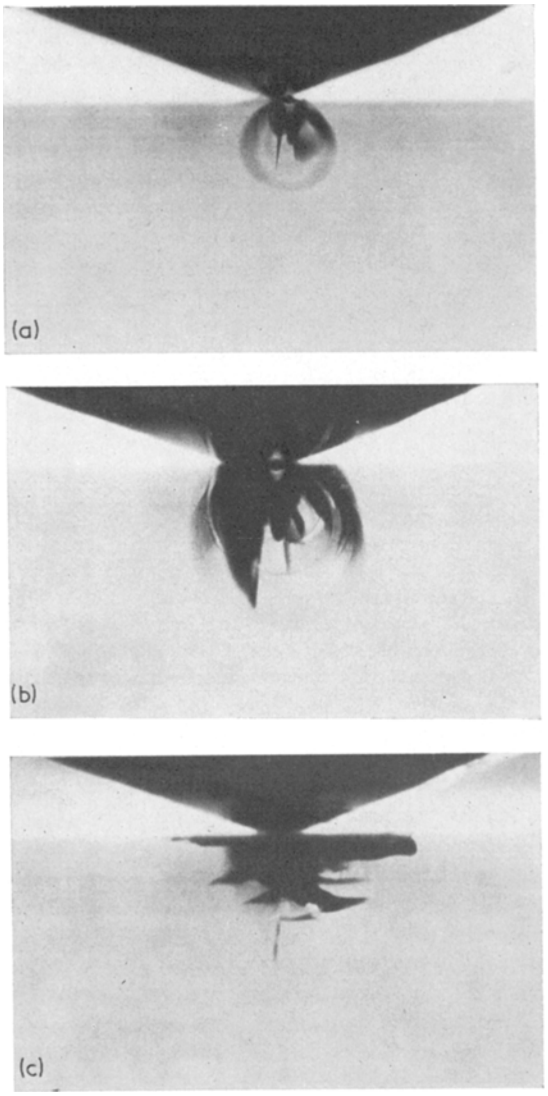

Figure 8 *In situ* photographs of Vickers indentation in soda-lime glass, taken in transmitted light. Specimen loaded to (a) 250 N, (b) 500 N, then unloaded to (c) zero. Note evidence in (b) for "breakthrough" of main median vent to surface, and for presence of second median vent (dark segment) inclined to line of vision. Width of field 11 mm.

stress σ_{22}, but is likely to be restricted in this sideways growth by the compressive lobes at $\phi > 51.8°$ in the σ_{22} field (Fig. 3b). These predictions accord well with the observed median vent profile shown in the micrograph of Fig. 8a. Thus, as long as the conditions of crack growth remain well defined, it would appear that we have the basis for a standard fracture mechanics analysis of the problem.

Before proceeding to this end, however, it is well to indicate briefly some of the observed complications in the crack pattern which might be expected to impose limitations on any quantitative analysis:

(i) In poorly prepared specimens the premature formation of Hertzian-type cracks (Fig. 9a) may partially suppress initiation of the median vent. This occurs when a surface flaw in the highly tensile 'skin' layer outside the contact area (Fig. 3a) becomes critical before the nucleation centre within the deformation zone itself, thence flaring downward and outward into a truncated near-cone fracture delineated by the σ_{22} and σ_{33} stress trajectories (Fig. 2) [6]. The crack pattern accordingly becomes more a function of surface history than of inherent deformation properties of the material. In most instances, due attention to indenter sharpness and specimen polishing was enough to prevent the incidence of such spurious cracking.

(ii) Further spurious cracking may eventuate under certain indenter-specimen interface conditions, particularly with tests on glass in water. The median vents are then ill-formed, and sometimes do not appear at all. In such cases bundles of splinter-like cracks tend to emanate from the deformation zone, and propagate stably downward along σ_{33} trajectories inclined to the contact axis (Fig. 2).

(iii) In many situations geometrical factors favour the formation of more than one median vent beneath the indenter. For instance, the sharp edges of a Vickers pyramid tend to initiate, in isotropic materials, mutually orthogonal, intersecting vents along the diagonals of the impression. This is seen in Fig. 8b. In a material such as monocrystalline lithium fluoride, on the other hand, the strong tendency to 'easy cleavage' on low-index planes becomes a dominant factor in determining vent orientations [7].

(iv) Discontinuities in the load-displacement characteristic are observed during indentation. Apart from an initial, small discontinuity at first appearance of the median vents, other, larger ones become apparent in advanced stages of growth as the sides of the vents suddenly break through the restraining compressive stress lobes to intersect the free surface. This 'breakthrough' accounts for the radial cracking commonly observed on heavily indented specimens (Fig. 9b).

(v) The lateral vents show even more complex geometrical behaviour than the median vents

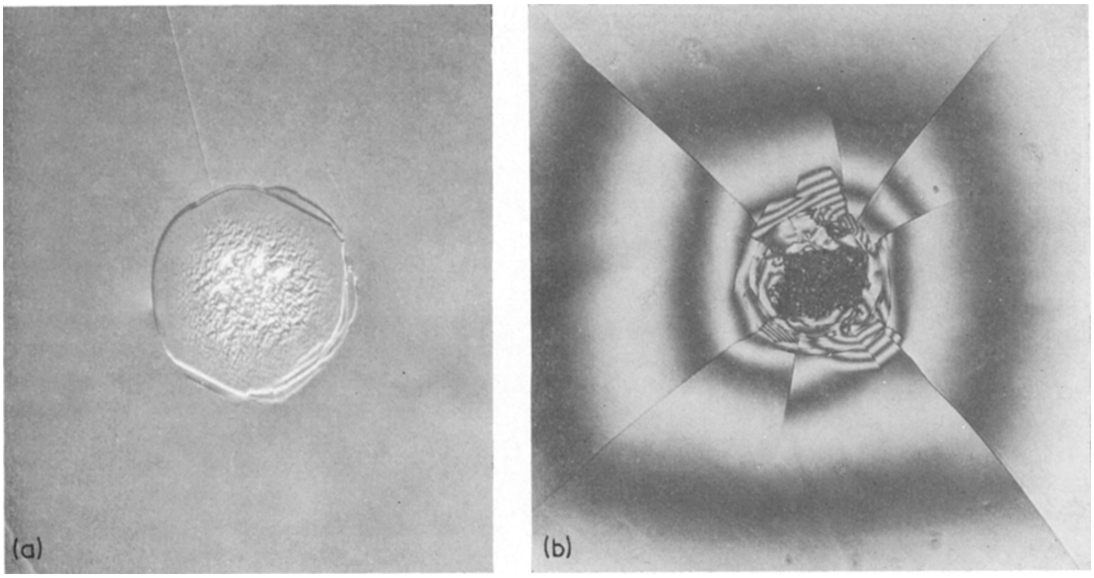

Figure 9 Residual crack patterns on indented silicon (111) surfaces. Conical indenter, included angle 160°. (a) Interference contrast micrograph, showing trace of near-cone crack; indenter load 20 N; width of field 100 μm; (b) interference fringe micrograph, showing traces of median vent cracks; indenter load 100 N; width of field 300 μm. Note deformation at centre of each indent.

(Fig. 8c). This type of cracking may occur regardless of whether the threshold for median vent initiation is exceeded, thereby demonstrating the vital role of the ill-defined residual stress system associated with the unloaded deformation zone.

(vi) The overall crack pattern is characterized by a certain time dependence, as manifested by the effects of rate of loading and unloading, nature of environment, etc. The observed behaviour appears to be consistent with the known enhancing effects of water (even in small traces) on both microcrack growth [8] and deformation processes within the hardness zone [9]. However, the effect is second order in this investigation, amounting to an increase of no more than a few percent in the size of the median vents after several min duration of applied load.

4. Fracture mechanics of median vent

We turn now from the question of crack *geometry* to the question of crack *stability*. In particular, we seek to quantify the scale of the microcracking in terms of the applied loading. Standard analytical 'fracture-mechanics' techniques are particularly useful here [5]. In principle, fracture mechanics should be capable of providing formal solutions for crack propagation in any specifiable stress field; however, in reality only the simplest crack configurations are mathematically tractable. Accordingly, bearing in mind the above-mentioned complicating features in the crack pattern, we can hope to go no further than a first-approximation treatment of the growth of a well-behaved median vent. Even then, gross simplifying assumptions must be introduced into the description of the crack evolution.

We begin by seeking a geometrical representation of the median vent crack for which a

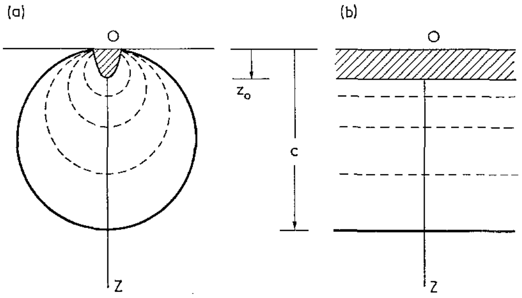

Figure 10 Fracture mechanics model for analysis of median vent propagation. Heavy line represents the crack profile (characteristic dimension c), broken lines the stress contours, and shading lines the deformation zone (characteristic dimension z_0). (a) Penny-shaped representation; (b) straight-fronted analogue.

standard fracture-mechanics solution is available. Our aim is to obtain an expression for the *stress-intensity factor* K (which gives a measure of the intensity of the stress field in the near vicinity of the crack tip) in terms of the indenter load P and characteristic crack dimension c (Fig. 10). Here it is of interest to compare solutions for two plane-crack configurations, the straight-fronted edge crack (with c the crack length) and the penny-shaped internal crack (with c the crack diameter). In a homogeneous stress field the stress-intensity factor for the second configuration is simply $\sqrt{2}/\pi$ times that for the first [5]; for the more general, inhomogeneous stress field, however, a suitable solution exists only for the straight-fronted crack. Thus the first step in establishing a model of the vent crack might be to regard the contours of prior tensile stress as a family of circles having a common plane θ = constant and common surface tangent at $R = 0$ (Fig. 3b), and the crack profile to be coincident with one of these circles (Fig. 8a). Then the second step would be to proceed by analogy with the homogeneous stress case, and to approximate the stress-intensity factor for the circular crack by $\sqrt{2}/\pi$ times that for the straight-fronted crack; the appropriate expression is [5]

$$K = \frac{2^{1/2}}{\pi}\left\{2\left(\frac{c}{\pi}\right)^{1/2}\int_0^c \frac{\sigma_{22}(z)\mathrm{d}z}{(c^2 - z^2)^{1/2}}\right\} \qquad (4)$$

with $\sigma_{22}(z)$ the relevant stress along the contact axis.

However, as already noted in Fig. 5, the stress distribution becomes uncertain as one approaches the contact zone: indeed, direct substitution of the Boussinesq field solution $\sigma_{22}(z) = \sigma_{\theta\theta}(z)$ (Appendix) into Equation 4 gives rise to an infinity in K. To overcome this difficulty we use the expedient of a 'cut-off depth', z_0 say, as a lower limit for the integration; this parameter may then be taken as a characteristic dimension of the deformation zone (Fig. 10), within which any tensile stresses might reasonably be expected to relax to zero. Equation 4 accordingly modifies to

$$K = \left(\frac{1 - 2\nu}{2^{1/2}\pi^{5/2}}\right) P c^{1/2} \int_{z_0}^{c} \frac{\mathrm{d}z}{z^2(c^2 - z^2)^{1/2}} \,. \qquad (5)$$

For most brittle materials, it is found that the median vent extends well below the damage region (Fig. 7), i.e. $c \gg z_0$. In this approximation, Equation 4 reduces to

$$K = (1 - 2\nu)P/2^{1/2}\pi^{5/2}z_0c^{1/2} \,. \qquad (6)$$

We may now make use of the geometrical similarity of the deformation zone (Section 2) to determine the manner in which z_0 varies with load. In conjunction with Equation 2 we write

$$z_0 = \beta a = \beta P^{1/2}/(\alpha\pi p_0)^{1/2}, \qquad (7)$$

where β is a dimensionless factor determined by zone geometry. Equation 6 then becomes

$$K = \left\{\frac{(1 - 2\nu)\,(\alpha p_0)^{1/2}}{2^{1/2}\pi^2\beta}\right\}\left(\frac{P}{c}\right)^{1/2} \,. \qquad (8)$$

From here it is a simple step to a fracture criterion [5]. We compute the *crack-extension force*, defined for plane-strain conditions by

$$G = (1 - \nu^2)K^2/E \,. \qquad (9)$$

Combining Equations 8 and 9 gives

$$G = \left\{\frac{(1 - \nu^2)\,(1 - 2\nu)^2\alpha p_0}{2\pi^4\beta^2 E}\right\}\frac{P}{c} \,. \qquad (10)$$

For growth under equilibrium conditions the driving force for the crack must just balance the resisting force (Griffith condition); that is,

$$G = 2\Gamma \,, \qquad (11)$$

where Γ is the *fracture surface energy*. Equating equations 10 and 11 gives finally,

$$\frac{P}{c} = \frac{4\pi^4\beta^2\Gamma E}{(1 - \nu^2)\,(1 - 2\nu)^2\alpha p_0} \,. \qquad (12)$$

The crack length is thus predicted to extend stably in proportion to the load.

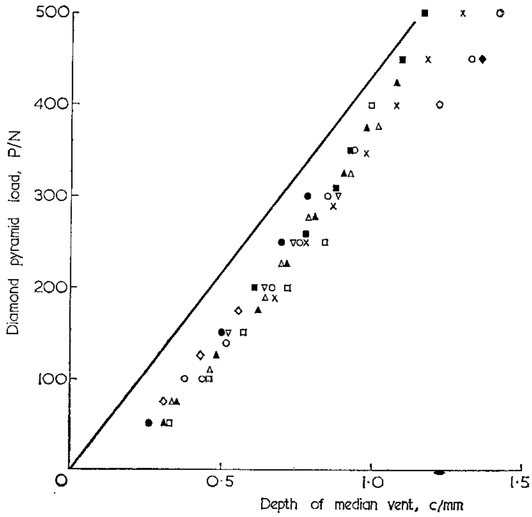

Figure 11 Theoretical plot (full line, Equation 12) and experimental plot (data points, optical observations with each symbol representing a different crack) of $P(c)$ for well-behaved median vent cracks in soda-lime glass indented with Vickers pyramid.

It is of interest to evaluate this relationship for some specific system, say for Vickers pyramid indentations on soda-lime glass (e.g. Fig. 8). We take the following typical values: $\alpha = 2/\pi$ (with a half-diagonal of indentation), $\beta = 2$ (taken as ratio depth/half-diagonal of deformation zone, Fig. 7), $E = 7 \times 10^{10}$ Nm^{-2}, $\nu = 0.25$, $\Gamma = 4$ Jm^{-2} (double-cantilever datum [10]), $p_0 = 6.5 \times 10^9$ Nm^{-2} (direct measurement of contact under load). Insertion into equation 12 gives $P/c = 4.4 \times 10^5$ Nm^{-1}. This result is plotted in Fig. 11 as the full line. Also plotted in Fig. 11 are data points representing direct observations of crack length as a function of applied load for several well-behaved vents. Agreement between theory and experiment is better than order-of-magnitude over the range of values covered, which is more than satisfactory considering the uncertainties in the indentation model.

5. Discussion

Our treatment above provides a descriptive basis for the more general features of point-indentation microfracture patterns in brittle solids. The formation of median vents on loading and lateral vents on unloading follows as a natural adjunct to the irreversible deformation processes which give rise to the residual hardness impression. Yet because the ultimate crack propagation depends on the stress situation over a distance large compared with the scale of the contact zone, we have been able to analyse the median vent mechanics in terms of the Boussinesq elastic field equations for point loading. This has given us, through a knowledge of the material constants in Equation 12, a means of predicting *a priori* the depth of fracture damage in terms of given applied loading conditions: conversely, it has given us a means of inferring the loading history from the measured depth of cracking. Such information can be of great value in the evaluation of surface fragmentation and cutting processes. Or again, given both loading situation and crack depth, we have the basis of a simple method for estimating the fracture surface energy: in the case of opaque solids, e.g. hard metals [11, 12] or even rocks, the extent of cracking may be quantified in terms of the surface traces of well-developed median vents [13].

On the other hand, our fracture mechanics analysis does not extend to the lateral vents. To analyse this phase of the microfracture process we would need to have detailed knowledge of the residual stress field imposed by the relaxing deformation zone on unloading. This presents itself as a formidable problem, requiring for a start a complete description of the mechanics of zone formation itself. Nevertheless, if we were to concern ourselves less with the question of the absolute lengths of the lateral vents, and more with the question of the degree of chipping *if* the vents intersect the surface, then some useful information might be obtained by once again invoking geometrical similarity. Thus, on the assumption that the volume of the potential chip must scale with that of the residual impression (Fig. 6f), we write $V = \kappa a_{\mathrm{m}}^3 = (\kappa^{2/3}/\alpha\pi p_0)^{3/2} P_{\mathrm{m}}^{3/2}$ (using Equation 2), where κ is a dimensionless constant to be determined empirically and the subscript m designates values at maximum indentation. This simple-minded approach might indeed be used to form the basis for a working model in certain surface fragmentation processes, where individual chipping events are represented as miniature point indentations [14].

It should finally be emphasized that in bypassing consideration of the micromechanisms within the irreversible deformation zone we have left unanswered many important questions concerning the initiation of the vent cracks. In particular, how do such variables as defect mobility (dislocations, point defects), nature of environment, load rate, etc. determine the critical conditions for crack nucleation? The answers to such questions may hold the key to the ultimate control of the micro-fracture patterns in a given brittle system. The practical implications are important here: for example, in glass-cutting, where smooth, damage-free edges are required, it is essential to propagate a single, well-formed, trailing median vent beneath and behind the moving cutting wheel, and simultaneously to suppress the formation of lateral vents or other spurious cracks; conversely, in fragmentation processes, where surface chipping needs to be optimized, it is the lateral vent configuration which must be preferentially developed.

Appendix

Solutions for the stress field in an elastic half-space under normal point loading, first derived in 1885 by J. Boussinesq, are available in standard texts on elasticity theory [15]. In terms of the curvilinear coordinates of Fig. 1 we have the following components;

$$\sigma_{rr} = \frac{P}{\pi R^2}\left\{\left(\frac{1-2\nu}{4}\right)\sec^2\frac{\phi}{2} - \tfrac{3}{2}\cos\phi\sin^2\phi\right\}$$

$$\sigma_{\theta\theta} = \frac{P}{\pi R^2}\left\{\left(\frac{1-2\nu}{2}\right)\left(\cos\phi - \tfrac{1}{2}\sec^2\frac{\phi}{2}\right)\right\}$$

$$\sigma_{zz} = \frac{P}{\pi R^2}\left\{-\tfrac{3}{2}\cos^3\phi\right\} \qquad \text{(A1)}$$

$$\sigma_{rz} = \frac{P}{\pi R^2}\left\{-\tfrac{3}{2}\cos^2\phi\sin\phi\right\}$$

$$\sigma_{r\theta} = \sigma_{\theta z} = 0\,.$$

Suitable tensor transformations provide the directions and magnitudes of the principal stress components. Two of the principal normal stresses, σ_{11} and σ_{33}, are contained in the symmetry plane θ = constant, their angles with the specimen surface given by

$$\tan 2\alpha = 2\sigma_{rz}/(\sigma_{zz} - \sigma_{rr})\,. \qquad \text{(A2)}$$

The third principal normal stress, σ_{22}, is everywhere perpendicular to the symmetry plane. The principal directions are labelled such that $\sigma_{11} \geqslant \sigma_{22} \geqslant \sigma_{33}$ generally. We then have (noting that $\sigma_{rz} \leqslant 0$ for all $0 \leqslant \phi \leqslant \pi/2$)

$$\begin{aligned}\sigma_{11} &= \sigma_{rr}\sin^2\alpha + \sigma_{zz}\cos^2\alpha - 2\sigma_{rz}\sin\alpha\cos\alpha\\ \sigma_{22} &= \sigma_{\theta\theta} \qquad \text{(A3)}\\ \sigma_{33} &= \sigma_{rr}\cos^2\alpha + \sigma_{zz}\sin^2\alpha + 2\sigma_{rz}\sin\alpha\cos\alpha\,.\end{aligned}$$

The principal shear stresses are accordingly given by

$$\begin{aligned}\sigma_{13} &= \tfrac{1}{2}(\sigma_{11} - \sigma_{33})\\ \sigma_{12} &= \tfrac{1}{2}(\sigma_{11} - \sigma_{22}) \qquad \text{(A4)}\\ \sigma_{23} &= \tfrac{1}{2}(\sigma_{22} - \sigma_{33})\,,\end{aligned}$$

inclined at $\pi/4$ to the principal directions. Lastly, the magnitude of the component of hydrostatic compression is

$$p = -\tfrac{1}{3}(\sigma_{11} + \sigma_{22} + \sigma_{33})\,. \qquad \text{(A5)}$$

Acknowledgements

We wish to acknowledge the vital role of the Fracture and Comminution group under the direction of Dr T. R. Wilshaw at the Division of Materials Science, Sussex University, in prompting this work. A UK Science Research Council Fellowship (B.R.L.) and an Australian Commonwealth Scholarship (M.V.S.) provided financial support.

References

1. A. KELLY, "Strong Solids" (Clarendon, Oxford, 1966).
2. D. TABOR, "Hardness of Metals" (Clarendon, Oxford, 1951).
3. M. T. HUBER, *Ann. Physik* **14** (1904) 153.
4. M. V. SWAIN, Ph.D. Thesis, University of New South Wales, 1973.
5. B. R. LAWN and T. R. WILSHAW, "Fracture of Brittle Solids" (Cambridge University Press, Cambridge, in press), Ch. 3.
6. F. C. FRANK and B. R. LAWN, *Proc. Roy. Soc. Lond.* **A299** (1967) 291.
7. M. V. SWAIN and B. R. LAWN, *Phys. Stat. Sol.* **35** (1969) 909.
8. F. B. LANGITAN and B. R. LAWN, *J. Appl. Phys.* **41** (1970) 3357.
9. R. E. HANNEMAN and J. H. WESTBROOK, *Phil. Mag.* **18** (1968) 151.
10. S. M. WIEDERHORN, *J. Amer. Ceram. Soc.* **52** (1969) 99.
11. D. J. ROWCLIFFE and G. E. HOLLOX, *J. Mater. Sci.* **6** (1971) 1261.
12. E. A. ALMOND and B. ROEBUCK, "Scanning Electron Microscopy: Systems and Applications" (Conference Proceedings, Institute of Physics, London, 1973) p. 106.
13. S. PALMQVIST, *Arch. Eisenhuttenwessen* **33** (1962) 629.
14. T. R. WILSHAW, G. M. CRIMES, K. PHILLIPS, W. SWINDLEHURST and I. FREEMAN, unpublished work.
15. J. BOUSSINESQ, "Application des Potentiels à l'Etude de l'Equilibre et du Mouvement des Solides Elastiques" (Gauthier-Villars, Paris, 1885), discussed in S. P. TIMOSHENKO and J. N. GOODIER, "Theory of Elasticity" (McGraw-Hill, New York, 1970) pp. 398-402.

Received 2 July and accepted 17 July 1974.